Relationship between subduction erosion and

the up-dip limit of the 2014 Mw 8.1 Iquique earthquake

Florian Petersen[1], Dietrich Lange[1], Bo Ma[1], Ingo Grevemeyer[1], Jacob Geersen[2], Dirk Klaeschen[1], Eduardo Contreras-Reyes[3], Sergio Barrientos[4], Anne M. Tréhu[5], Emilio Vera[3], and Heidrun Kopp[1,2]

[1]GEOMAR Helmholtz Centre for Ocean Research Kiel, Kiel, Germany

[2]Institute of Geosciences, Kiel University, Kiel, Germany

[3]Departamento de Geofísica, Facultad de Ciencias Físicas y Matemáticas, Universidad de Chile, Santiago, Chile

[4]Centro Sismológico National, Facultad de Ciencias Físicas y Matemáticas, Universidad de Chile, Santiago, Chile

[5]Oregon State University, College of Earth, Ocean, and Atmospheric Sciences, Corvallis, USA

Contents of this file

Text S1 to S9
Figures S1 to S12

Introduction

This appendix provides supporting information on the methods we used to investigate the local seismicity following the 2014 Mw 8.1 Iquique earthquake. We used the continuous waveform data from two subsequent Ocean Bottom Seismometer installations and the permanent land stations from CSN (Barrientos, 2018) and IPOC (GFZ & CNRS-INSU, 2006) between December 9, 2014, and October 31, 2016. Our local seismic catalog covers the region between 72° W and 69.5°W and between 22°S and 19°S. In total, the amphibious catalog comprises 1,990 earthquakes observed on at least eight stations (Figure S1), including 27,877 P-phase picks and 7,229 S-phases. The entire seismic catalog and waveform data are available from the PANGAEA archive (https://www.pangaea.de). The local magnitude of completeness is Ml 1.75 in the first year and Ml 2.5 in the second year. The decrease in the magnitude of completeness results from less operating OBS in the second year.

S1 Earthquake detection and picking of P-phases

Earthquakes were detected with the scanloc module of SeisComP3 (GFZ & GEMPA, 2008) using a cluster search algorithm to associate phase detections to one or many potential earthquake sources. Source scanning was done with the local 1-D velocity model from Husen et al. (1999) (Figure S3). In the next step, the SeisComP3 estimated P-phase picks were used to re-pick P-phases onsets using the automatic Manneken Pix (MPX) algorithm (Aldersons, 2004) following the procedure of (Lange et al., 2012). All phase picks manually

revised and associated with uncertainty from 0 to 4 according to their quality and re-picked using the SEISAN software (Havskov et al., 2020).

S2 Picking of S-phases

In the next step, S-phases were picked for all events with more than 8 P picks using the S-phase pick algorithm of Diehl et al. (2009). All phase picks are associated with uncertainty from 0 to 4 according to their quality, and we removed all phases with a ratio of station residual to epicentral distance higher than 0.05 s/km. However, automated phase picking on OBS data turned out to be unsatisfactory due to increased noise on the waveform data. Hence, we manually revised the phase picks on the OBS data.

S3 1D minimum Velocity Model

We selected 520 events from our local earthquake catalog with a gap of less than 180° and more than 12 P-wave arrivals and 8 S-wave arrivals to calculate local one-dimensional (1D) vp models and 1D vp/vs velocity models. The inversion is performed with VELEST (Kissling et al., 1995) using the staggered approach for inverting vp and vp/vs 1D velocity models (Husen et al., 1999) using a wide range of input velocity models (e.g., Sielfeld et al., 2019). The 1D velocity models are shown in Figure S3.

S4 2D-tomography

The 1D models are then used as input for the 2D local earthquake tomography (LET) using SIMUL2000 (e.g., Thurber, 1983, 1992) following the procedure of Collings et al. (2012).

The earthquake locations from the minimum 1D velocity model and the one-dimensional input velocity model were used for the 2D tomography (Figure S5). The resolution matrix contains at each row an averaging vector for a single model parameter and reflects how individual model parameters are dependent on all other model parameters (Collings et al., 2012). High resolution and large diagonal elements result in a low spread value (Figure S6). The two-dimensional tomography resolution indicates good resolution for the updip region and the coastal area for both *vp* and *vp/vs*. The marine forearc basin is poorly resolved because of a small amount of shallow seismic activity and no station coverage. The 2D velocity model was used to relocate the entire catalog using NonLinLoc (Lomax et al., 2000).

S5 Magnitudes

We calculated moment magnitudes after Ottemöller and Havskov (2003) using standard values for geometric spreading and local magnitudes after Hutton and Boore (1987) using the maximum amplitudes of horizontal components of OBS and land stations. The instrument responses of OBS sensors are calibrated to match event magnitudes from land stations of the CSN (Figure S9) and result in similar magnitudes.

S6 Earthquake locations and uncertainties

Hypocenter locations were determined using the non-linear oct-tree search algorithm NonLinLoc (Lomax et al., 2000). The maximum likelihood location is chosen as the

preferred location from the probability density functions of event scatter samples. Furthermore, the oct-tree algorithm estimates hypocenter uncertainties based on a 3D error ellipsoid (68% confidence). The distribution of the obtained location errors was averaged in the latitude, longitude and depth for all the events within each of the spatial 0.1°x0.1° grid cells in which we subdivided the study region. To classify hypocenter locations in best (A), good (B), and fair (C) events, we use the procedure from Husen & Smith, 2004. We only consider the highest two classes, A and B with the most reliable earthquake locations (Husen & Smith, 2004).

S7 Double-difference locations

To obtain precise relative relocations and to investigate the internal seismicity structure of the marine forearc, we applied the double-difference algorithm (HypoDD, Waldhuser & Ellsworth, 2000) on our local earthquake catalog with events relocated using the 2D local earthquake tomography (section S4). The algorithm minimizes the residual between observed and theoretical travel time differences based on waveform cross-correlations between two nearby earthquakes at the same station that recorded both events. Cross-correlations for events pairs with calculated time differences are considered with a maximum distance of 10 km and a cross-correlation coefficient greater than 0.8. The local catalog now encompasses 916 earthquakes relocated using the double-difference algorithm HypoDD (Waldhuser & Ellsworth, 2000) and 862 earthquakes located using the non-linear oct-tree search algorithm NonLinLoc (Lomax et al., 2000) with the quality classes A and B (Husen & Smith, 2004)..

S8 Catalog comparison

The aftershock seismic catalog presented here overlaps in 23 days with the local seismicity catalog from Soto et al. (2019), starting on December 9, 2014, with the deployment of the first Ocean Bottom Seismometer (OB01) (Figure S8). We compared both catalogs and searched the OBS data for missing events by comparing the origin times. Both catalogs have 425 events in common, but we could not locate 25 events from Soto et al. (2019) in our OBS data (Figure S8) due to a low signal-to-noise ratio on OBS waveforms. Our OBS network detected additional 58 events missing in the catalog from Soto et al. (2019). These 58 events are mainly located offshore at the seismogenic up-dip limit. In contrast, the 25 events observed only by Soto et al. (2019) are primarily located in the down-dip region of the Iquique earthquake. The earthquake locations from the Soto et al. (2019) catalog are biased 1.6±0.04 km southwards, 3.27±0.02 km westwards and 0.9±0.06 km in depth relative to the locally determined hypocenters (Figure S8).

S9 Focal mechanisms

Focal mechanisms of 98 events are calculated based on revised first motion P phase polarities of events with more than 20 P polarities (FPFIT, Reasenberg et al., 1985). Unique solutions are considered, which are based on event azimuths and take-off angles from hypocenters. Besides, we used focal mechanisms from the Global Centroid Moment Tensor (gCMT) catalog (www.globalcmt.org) (Dziewonski et al., 1981; Ekström et al., 2012), which

comprises 20 earthquakes (Mw > 4.7) that occurred during the two years of the OBS deployment. CMT and focal mechanisms of the marine forearc are shown in Figure S10. In addition, we compared the focal mechanisms from FPFIT with three larger events of the global CMT catalog. We identified the largest discrepancy in the strike angle of the focal mechanisms (Figure S12). We calculated the bias in location as a weighted average for the events that the gCMT catalog and the local aftershock catalog have in common to compare the focal mechanism locations. The global gCMT catalog is displaced by 25±0.5 km in the North direction and 2.9 ± 0.5 km in the East direction and 8 km deeper relative to our local catalog based on amphibious data.
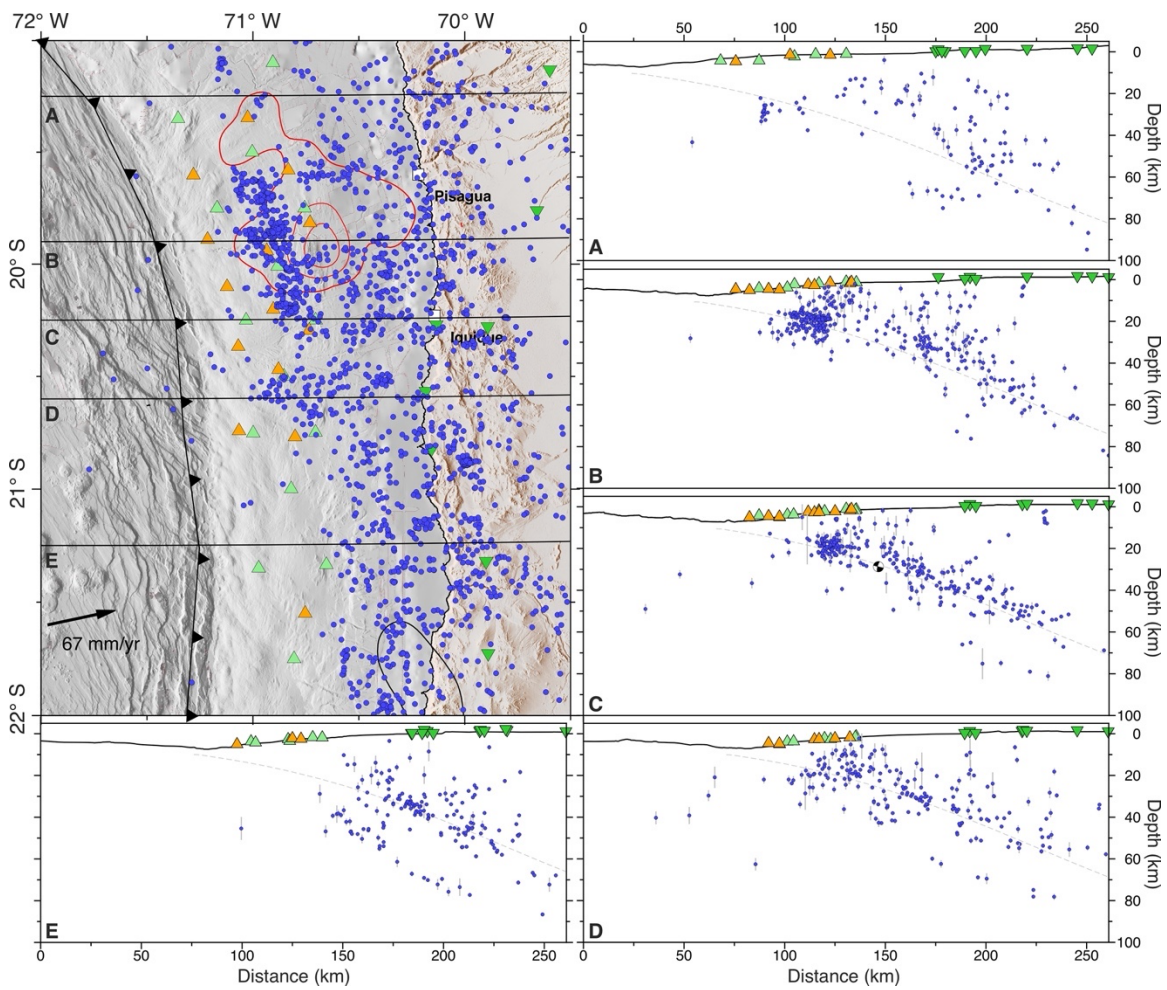
Figure S1. (Left) Map view of the total seismic catalog from December 9, 2014, until October 31, 2016. Coseismic slip model from Duputel et al. (2015) (Right) Profiles A-C crossing the rupture area of the 2014 Iquique earthquake. Blue dots indicate earthquakes located within the two-dimensional local earthquake tomography velocity model. Triangles mark the locations of the OBS deployments and land stations of CSN/IPOC, respectively.
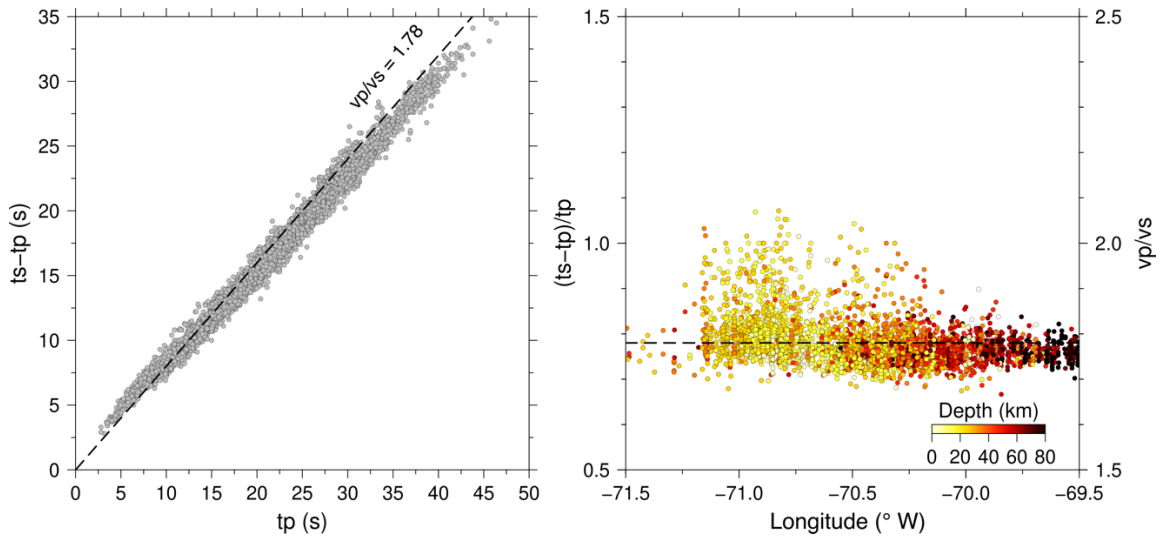
Figure S2. *(Left) Wadati diagram of all events detected OBS06, located in the center of the OBS network. The dashed line marks the vp/vs ratio of 1.78. (Right) Plot of vp/vs ratios versus hypocenter longitudes (e.g., Haberland et al., 2009). Events east of 70.5°W show an increase in the vp/vs ratio.*
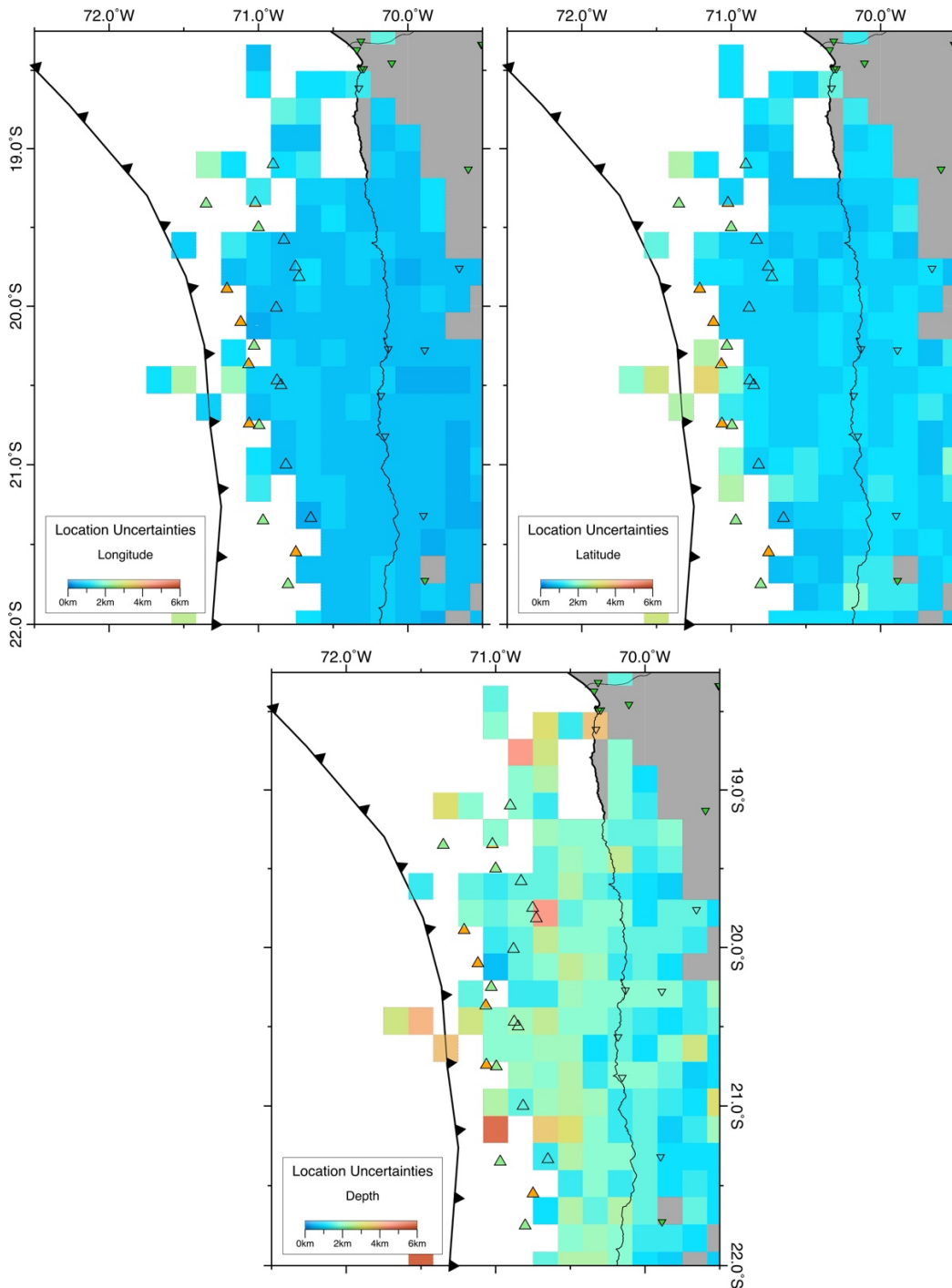
Figure S3. *Location uncertainties from average event locations for hypocenters at 0–60 km depth for 0.25×0.25° squares. Uncertainties estimated using the oct-tree algorithm of the probabilistic location scheme of NonLinLoc. Error ellipsoids (68% confidence) in three components x (longitude), y (latitude) and z (depth). Depth errors for shallow events outside the station network are not comparable to the large horizontal errors as the oct-tree search algorithm only explores the PDF within the pre-defined grid (e.g., no air-quakes).*
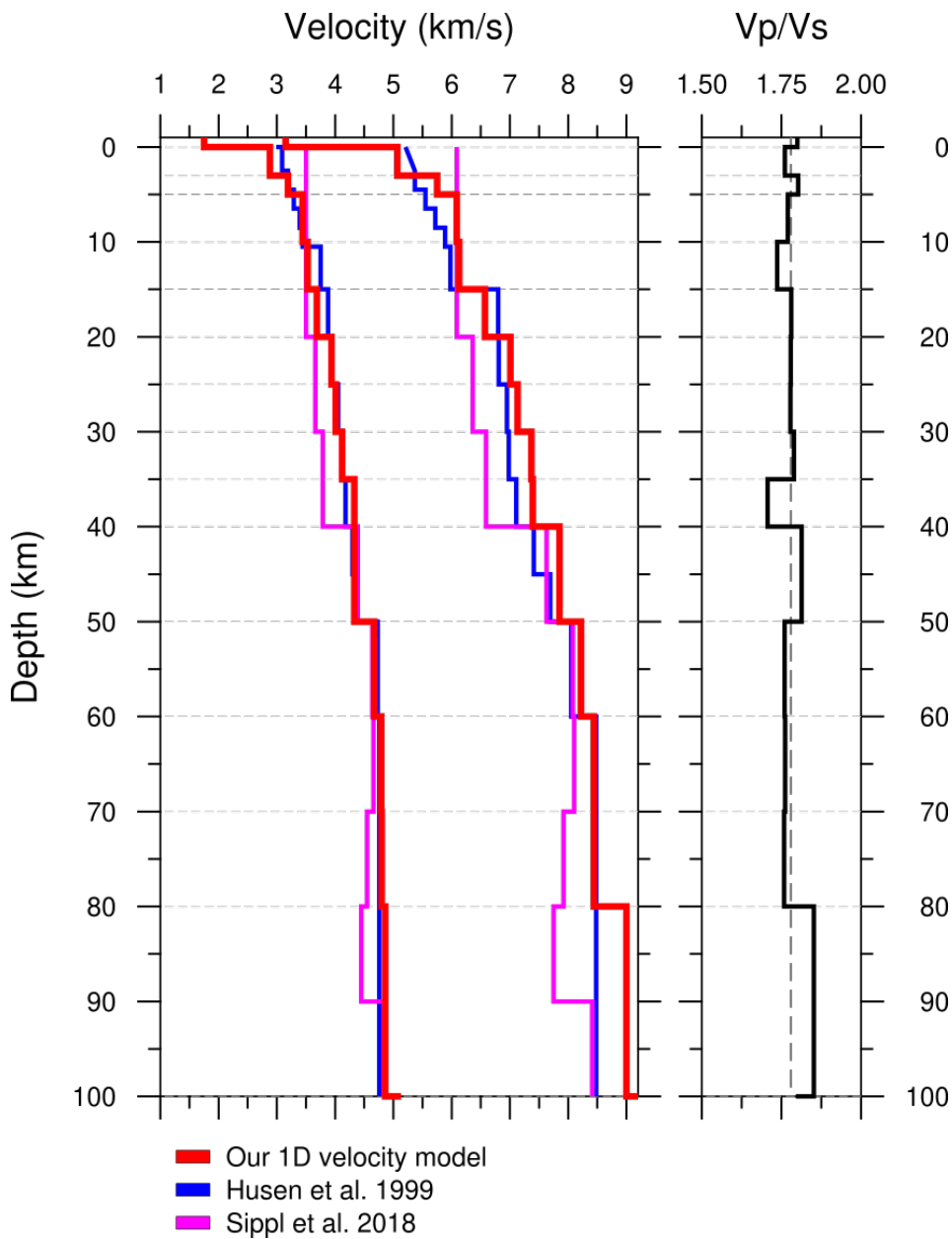
Figure S4. *Minimum 1D velocity model for the marine forearc. The red line indicates the velocity model calculated with the offshore recorded Iquique aftershock sequence determined using VELEST(Kissling et al., 1995). The upper layers up to 15 km are not well constrained due to the near-vertical ray paths below the seismic network (Husen et al., 1999; Sippl et al., 2018).*
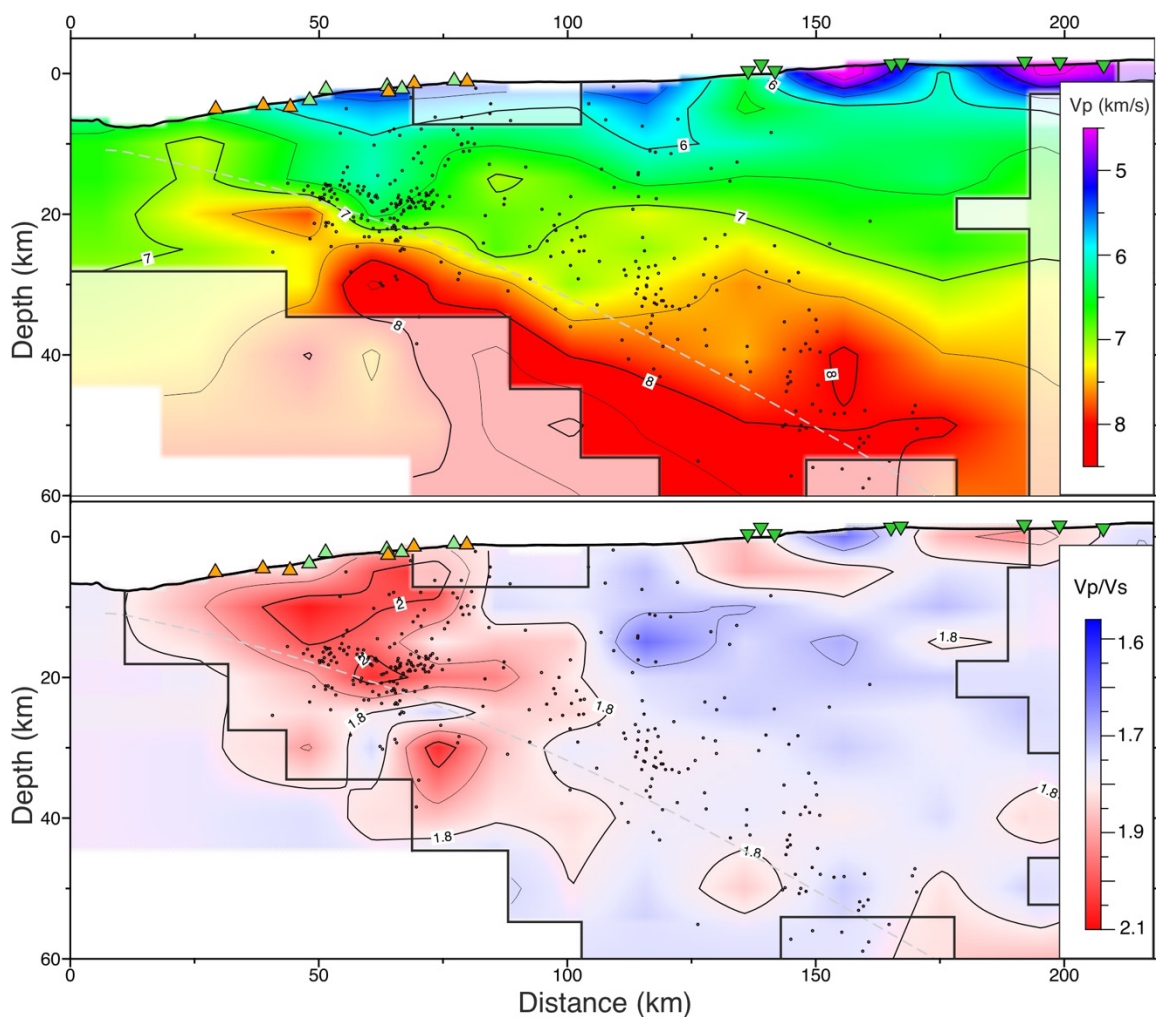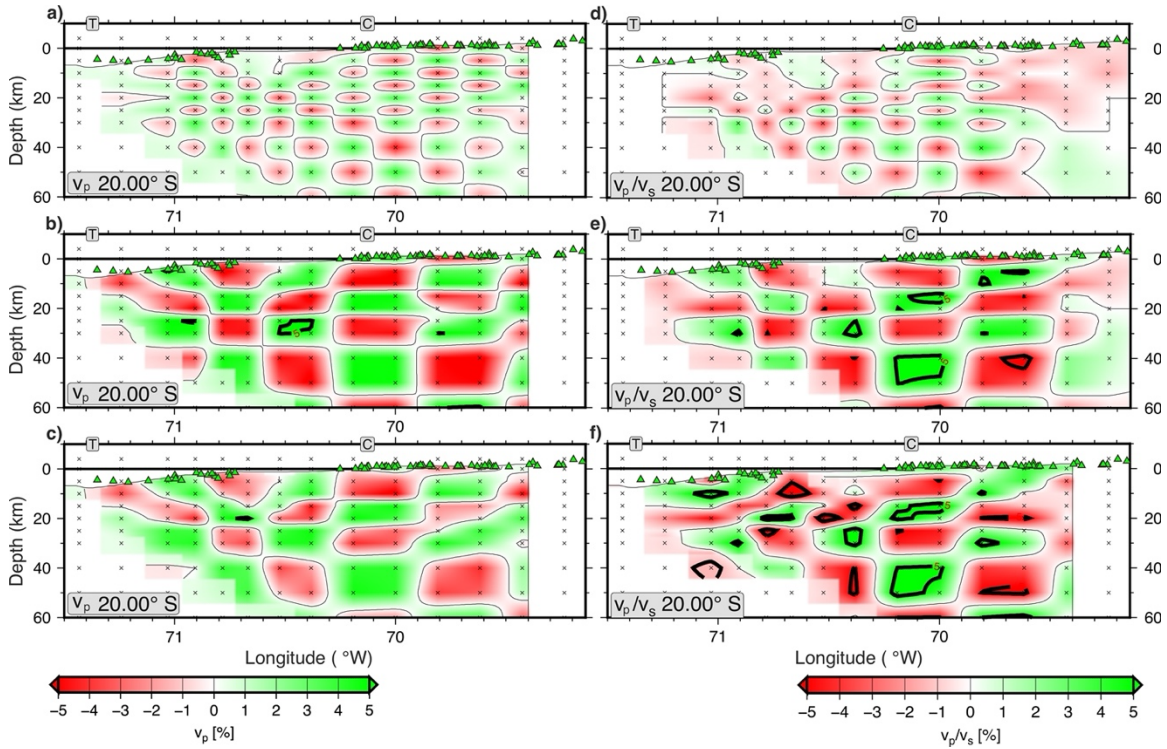
Figure S5. *Local earthquake tomography at 20°S west to east starting at 71.49°W using SIMUL2000 (e.g., Thurber, 1983) and aftershock seismicity. The grey dashed line indicated the Slab2 model by (Hayes et al., 2018). OBS locations on the marine forearc are marked as triangles with defined color codes as in Figure 1 of the main manuscript. (Top) the vp model, (Bottom) vp/vs ratio. Black solid line encircles the region of good resolution*
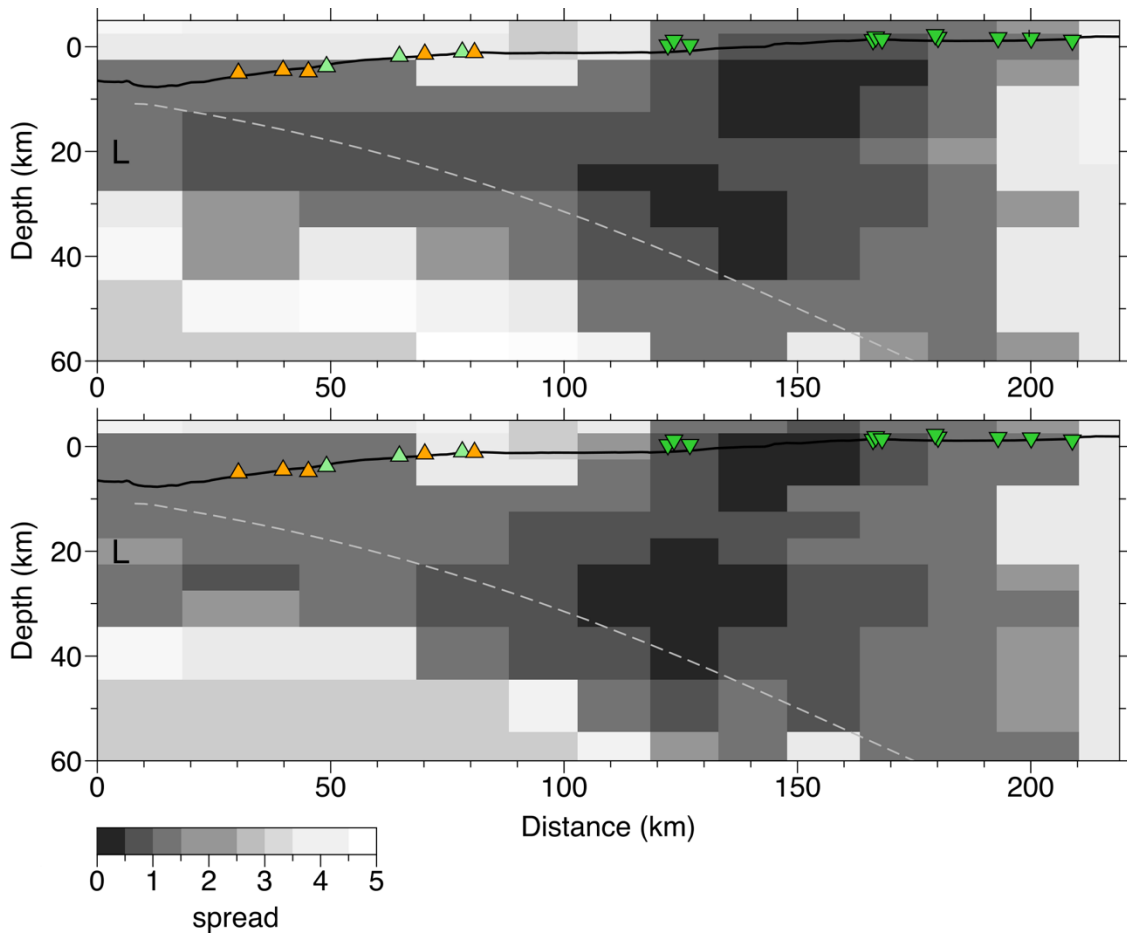
**Figure S6.** *Spread of the two-dimensional local earthquake tomography model for vp (top) and vp/vs (bottom). Estimates are based on the analysis of the resolution matrix with gray shading following the spread function values.*

Figure S7. *Checkerboards from the 2D local earthquake tomography. The profiles are oriented east west at 20°S. Stations are shown with green triangles at their real depths (projected onto the profile at 20°S. Contours lines exceeding the 5% of the input checkerboard are indicated with black thick lines and are labelled. Nodes are indicated with crosses. The location of the coast (trench) is marked with C and T, respectively. (Left) a) 1x1 checkerboard test vp, without noise; b) 2x2 checkerboard test vp, without noise; c) 2x2 checkerboard test vp, with noise dependent on the uncertainties of the different qualities of the picked phases. (Right) d) 1x1 checkerboard test vp/vs, without noise; e) 2x2 checkerboard test vp/vs, without noise; f) 2x2 checkerboard test vp/vs, with noise dependent on the uncertainties of the different qualities of the picked phases.*
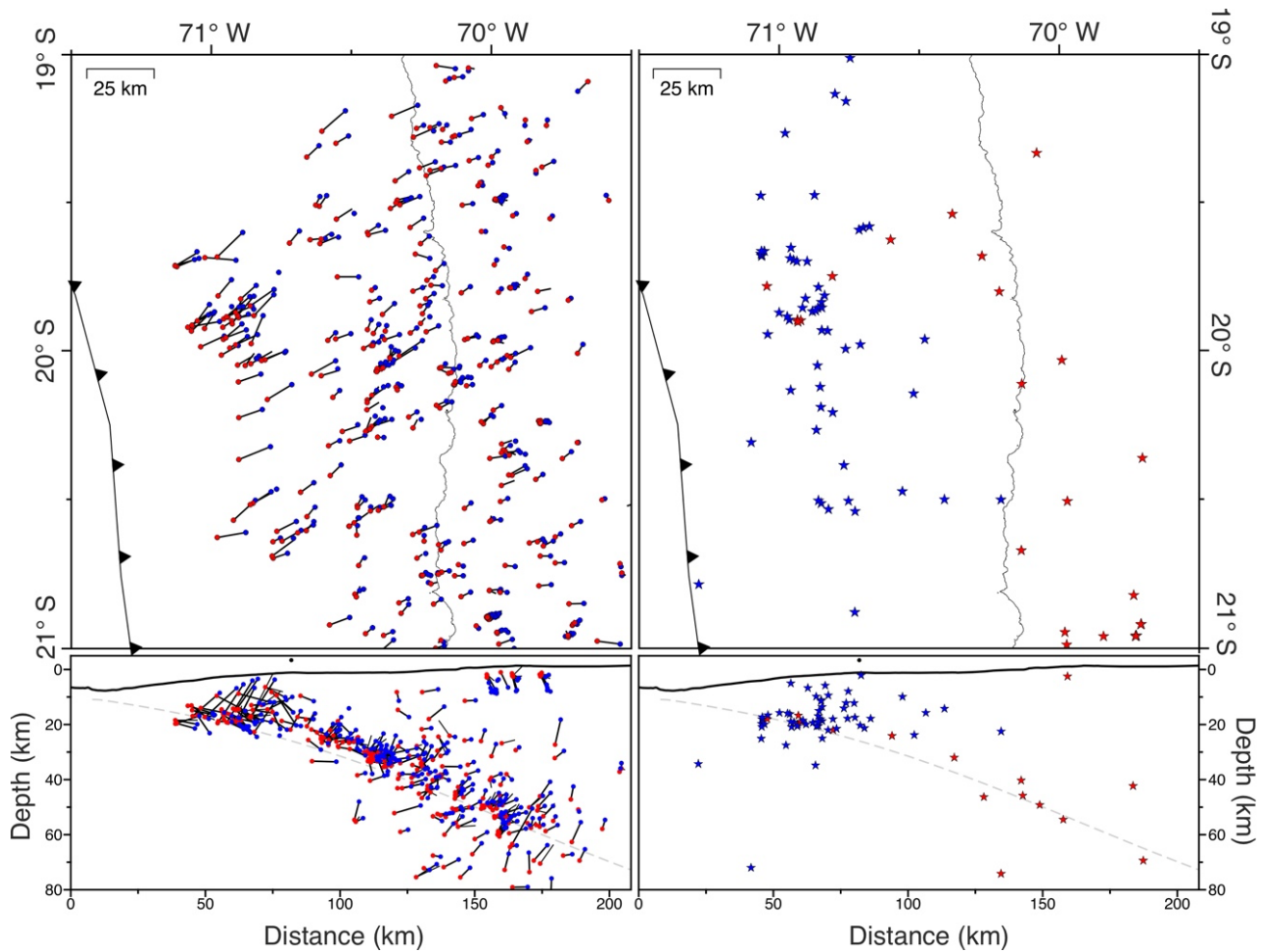
Figure S8. *Difference between the OBS catalog of this study (blue dots/stars) and the catalog based on land stations from Soto et al. (2019) (red dots/stars). Both Catalogs overlapping 23 days in December 2014 and have 425 in common. (Right) Common events in both catalogs with the epicentral difference displayed as a black line. (Left) Blue stars indicate event locations that appear only in the amphibious catalog and red stars indicate event locations in the catalog of Soto et al. (2019).*
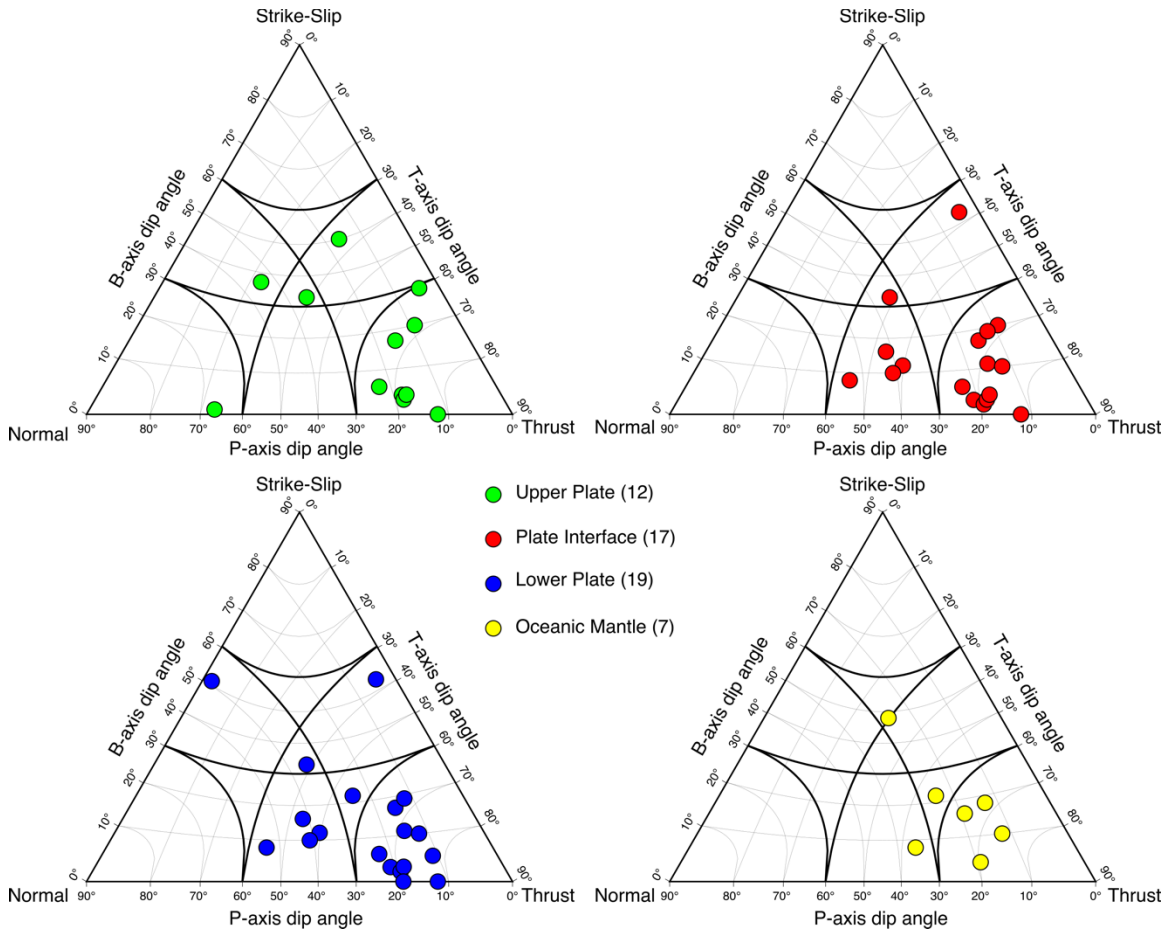
15
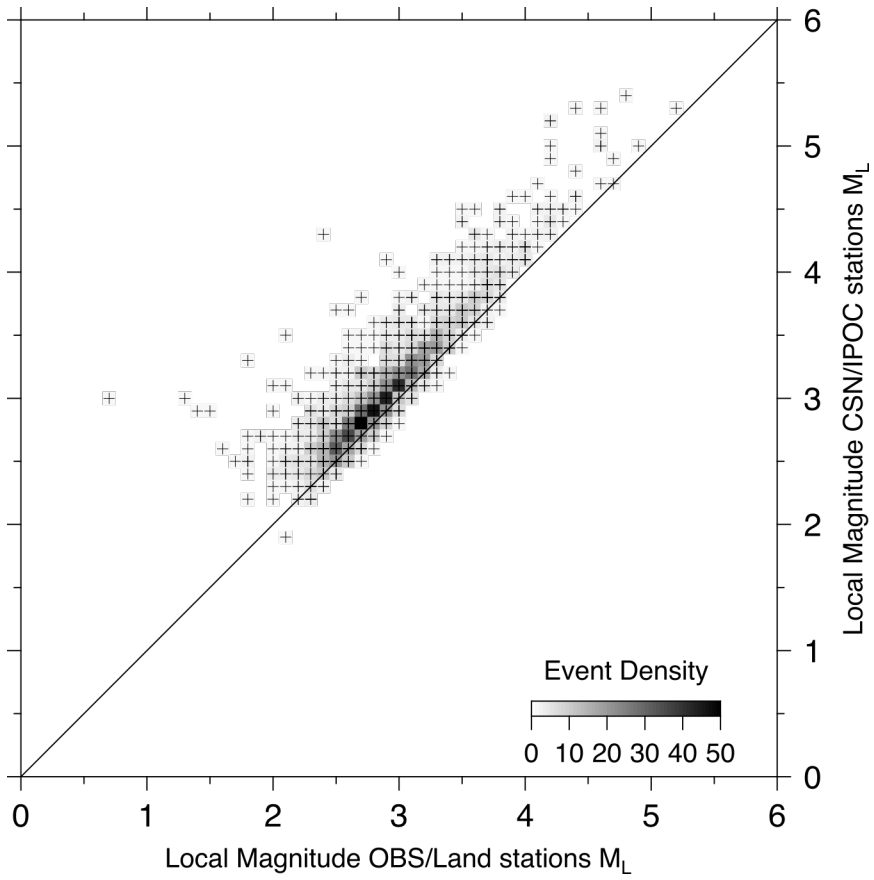
Figure S9. *Local magnitudes of our catalog versus the local magnitudes of the CSN catalog (Barrientos, 2018).*
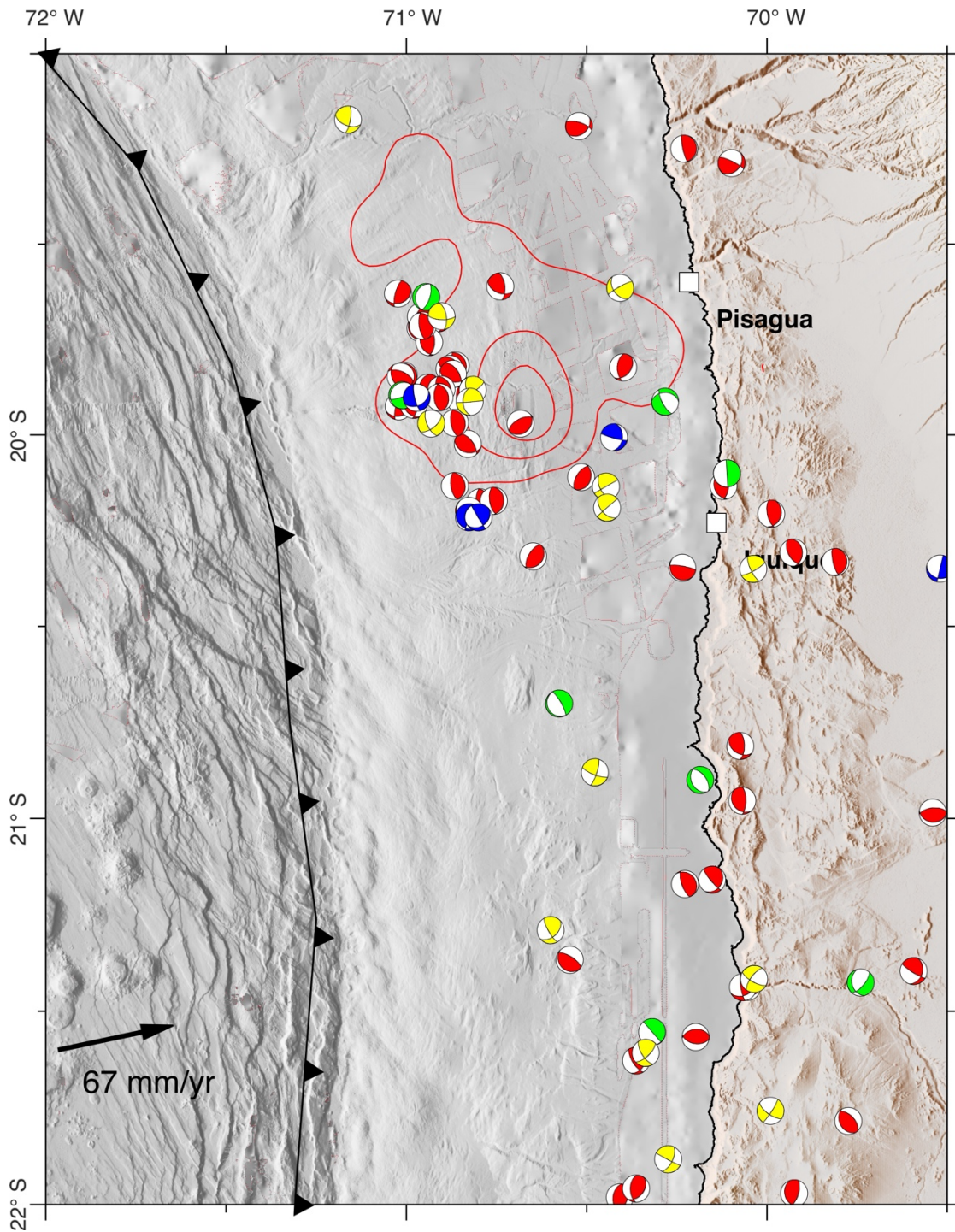
**Figure S10:** Focal mechanisms from FPFIT shown together with moment tensors from the gCMT catalogs (www.globalcmt.org). Beachballs are color-coded by faulting type in thrust (red), normal (green), strike-slip (yellow), or oblique (blue) fault mechanisms.

Figure S11. *Ternary azimuthal gnomonic projection for the classification of focal mechanisms (Frohlich, 1992). Red circles indicate earthquakes with vertical distances to the plate interface of 5 km on either side of the plate interface of the global Slab2 model (Hayes et al., 2018). Blue circles are focal mechanisms of earthquakes in the subducting lower plate and orange circles are focal mechanisms deeper 10 km below the global Slab2 model.*
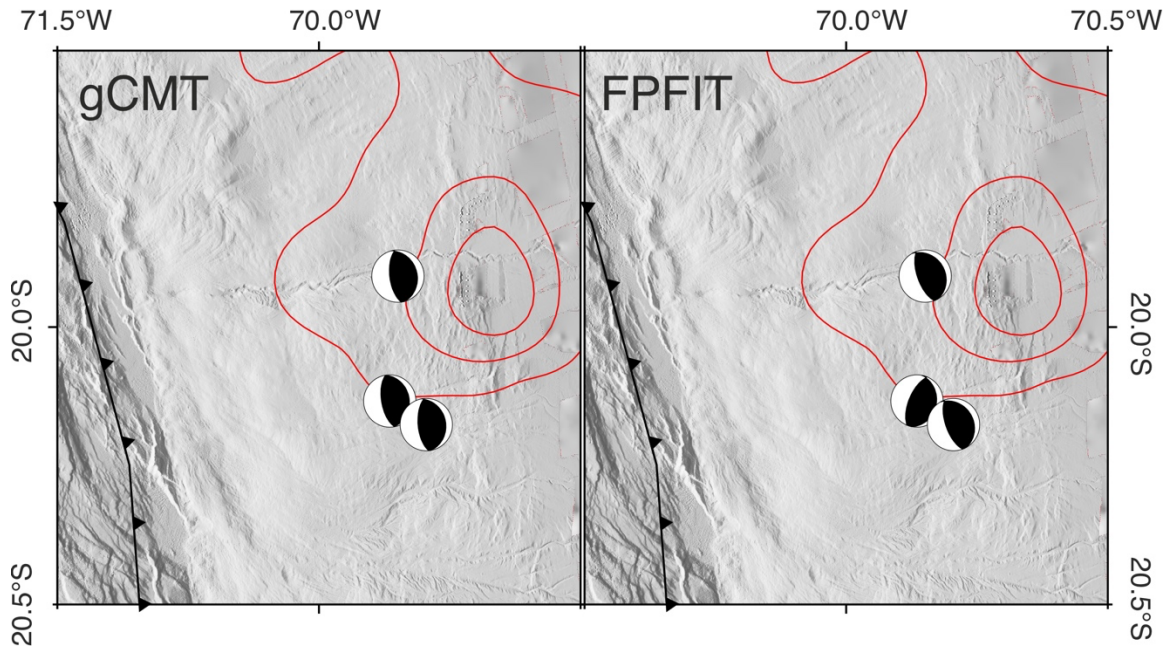
Figure S12. *Comparison of focal mechanisms between the (left) global gCMT catalog solutions and (right) our FPFIT solutions (Reasenberg & Oppenheimer 1985).*

References

Aldersons, F. (2004). *Toward a Three-Dimensional Crustal Structure of the Dead Sea region from Local Earthquake Tomography.* (Ph.D. thesis), Tel-Aviv University, Isreal.,

Barrientos, S. (2018). The Seismic Network of Chile. *Seismological Research Letters, 89*(2A), 467-474. doi:10.1785/0220160195

Collings, R., Lange, D., Rietbrock, A., Tilmann, F., Natawidjaja, D., Suwargadi, B., Miller, M., & Saul, J. (2012). Structure and seismogenic properties of the Mentawai segment of the Sumatra subduction zone revealed by local earthquake traveltime tomography. *Journal of Geophysical Research: Solid Earth, 117*(B1). doi:10.1029/2011jb008469

Diehl, T., Deichmann, N., Kissling, E., & Husen, S. (2009). Automatic S-Wave Picker for Local Earthquake Tomography. *Bulletin of the Seismological Society of America, 99*(3), 1906-1920. doi:10.1785/0120080019

Duputel, Z., Jiang, J., Jolivet, R., Simons, M., Rivera, L., Ampuero, J. P., Riel, B., Owen, S. E., et al. (2015). The Iquique earthquake sequence of April 2014: Bayesian modeling accounting for prediction uncertainty. *Geophysical Research Letters, 42*(19), 7949-7957. doi:10.1002/2015gl065402

Dziewonski, A. M., Chou, T. A., & Woodhouse, J. H. (1981). Determination of earthquake source parameters from waveform data for studies of global and

regional seismicity. *Journal of Geophysical Research: Solid Earth, 86*(B4), 2825-2852. doi:10.1029/JB086iB04p02825

Ekström, G., Nettles, M., & Dziewoński, A. M. (2012). The global CMT project 2004–2010: Centroid-moment tensors for 13,017 earthquakes. *Physics of the Earth and Planetary Interiors, 200-201*, 1-9. doi:10.1016/j.pepi.2012.04.002

GFZ, & CNRS-INSU. (2006). IPOC Seismic Network. Integrated Plate boundary Observatory Chile - IPOC. *Other/Seismic Network*. doi:10.14470/ PK615318

Haberland, C., Rietbrock, A., Lange, D., Bataille, K., & Dahm, T. (2009). Structure of the seismogenic zone of the southcentral Chilean margin revealed by local earthquake traveltime tomography. *Journal of Geophysical Research: Solid Earth, 114*(B1). doi:10.1029/2008jb005802

Havskov, J., Voss, P. H., & Ottemöller, L. (2020). Seismological Observatory Software: 30 Yr of SEISAN. *Seismological Research Letters, 91*(3), 1846-1852. doi:10.1785/0220190313

Hayes, G. P., Moore, G. L., Portner, D. E., Hearne, M., Flamme, H., Furtney, M., & Smoczyk, G. M. (2018). Slab2, a comprehensive subduction zone geometry model. *Science, 362*(6410), 58-61. doi:10.1126/science.aat4723

Husen, S., Kissling, E., Flueh, E. R., & Asch, G. (1999). Accurate hypocentre determination in the seismogenic zone of the subducting Nazca Plate in northern Chile using a combined on-/offshore network. *Geophysical Journal International, 138*(3), 687-701. doi:10.1046/j.1365-246x.1999.00893.x

Husen, S., & Smith, R. B. (2004). Probabilistic Earthquake Relocation in Three-Dimensional Velocity Models for the Yellowstone National Park Region, Wyoming. *Bulletin of the Seismological Society of America, 94*(3), 880–896. doi:10.1785/0120030170

Hutton, L. K., & Boore, D. M. (1987). The ML Scale in Southern California. *Bulletin of the Seismological Society of America, 77*(6), 2074-2094. 6

Kissling, E., Kradolfer, U., & Maurer, H. (1995). *Program VELEST user's Guide-Short Introduction*. Institute of Geophysics, ETH Zuerich.

Lange, D., Tilmann, F., Barrientos, S. E., Contreras-Reyes, E., Methe, P., Moreno, M., Heit, B., Agurto, H., et al. (2012). Aftershock seismicity of the 27 February 2010 Mw 8.8 Maule earthquake rupture zone. *Earth and Planetary Science Letters, 317-318*, 413-425. doi:10.1016/j.epsl.2011.11.034

Lomax, A., Virieux, J., Volant, P., & Berge-Thierry, C. (2000). Probabilistic Earthquake Location in 3D and Layered Models. In *Advances in Seismic Event Location* (Vol. 18, pp. 101-134).

Ottemöller, L., & Havskov, J. (2003). Moment Magnitude Determination for Local and Regional Earthquakes Based on Source Spectra. *Bulletin of the Seismological Society of America, 93*(1), 203-214. doi:10.1785/0120010220

Reasenberg, P., Oppenheimer, D., & USGS. (1985). *FPFIT, FPPLOT and FPPAGE Fortran computer programs for calculating and displaying earthquake fault-plane solutions*. U.S. Geol. Surv. Open-File Report. 85-739.

Sielfeld, G., Lange, D., & Cembrano, J. (2019). Intra-Arc Crustal Seismicity: Seismotectonic Implications for the Southern Andes Volcanic Zone, Chile. *Tectonics, 38*(2), 552-578. doi:10.1029/2018tc004985

Sippl, C., Schurr, B., Asch, G., & Kummerow, J. (2018). Seismicity Structure of the Northern Chile Forearc From >100,000 Double-Difference Relocated Hypocenters. *Journal of Geophysical Research: Solid Earth, 123*(5), 4063-4087. doi:10.1002/2017jb015384

Soto, H., Sippl, C., Schurr, B., Kummerow, J., Asch, G., Tilmann, F., Comte, D., Ruiz, S., et al. (2019). Probing the Northern Chile Megathrust With Seismicity: The 2014 M8.1 Iquique Earthquake Sequence. *Journal of Geophysical Research: Solid Earth, 124*(12), 12935-12954. doi:10.1029/2019jb017794

Thurber, C. H. (1983). Earthquake locations and three-dimensional crustal structure in the Coyote Lake Area, central California. *Journal of Geophysical Research, 88*(B10). doi:10.1029/JB088iB10p08226

Thurber, C. H. (1992). Hypocenter-velocity structure coupling in local earthquake tomography. *Physics of the Earth and Planetary Interiors, 75*(1-3), 55-62. doi:10.1016/0031-9201(92)90117-e

Waldhuser, F., & Ellsworth, W. L. (2000). A Double-difference Earthquake location algorithm Method and application to the Northern Hayward Fault, California. *Bulletin of the Seismological Society of America, 90*(6), 1253-1368. doi:10.1785/0120000006